

Bachelor Thesis

ADSORPTION OF ORGANIC MOLECULES ON AG(100)
AND MGO(100)/AG(100)

For the attainment of the degree Bachelor of Science (B.Sc.)
from the Institute of Physics at University of Graz.

Aleksey Sokolov

Matr.: 12004091



Supervisor: Univ.-Prof. Sterrer

Graz, September 2023

Abstract

Since the development of the Scanning Tunneling Microscope (STM) in 1981 it was used to get an insight into the electronic structure of molecules. [2] Especially the adsorption of organic molecules on metal or metal-oxide substrates peaked interest in the STM-Imaging field because of their semiconducting properties and their capacity for self-assembly. Additionally they promise cheap, flexible and tunable alternatives to conventional inorganic semiconductors in electronic and optoelectronic engineering fields [14]. In this thesis two adsorbates are studied using Scanning Tunneling Microscopy: Pentacenequinone and 2-Hydrogen-Phthalocyanine which fall into this category and are extensivly researched [21][18][20][8]. The primary objective of this thesis is to comprehend and classify the adsorption characteristics of those two molecules on Ag(100), and for 2HPC also on ultrathin MgO(100) layers grown on Ag(100).

Contents

1	Introduction	1
2	Fundamentals	3
2.1	Scanning Tunneling Microscopy (STM)	3
2.1.1	Theoretical Foundations of STM	5
2.2	Low Energy Electrons Diffraction (LEED)	7
2.3	Energy Alignment	9
2.3.1	Push-Back	11
2.3.2	Polarization	11
2.3.3	Charge-Transfer (CT)	11
3	Experimental Setup	13
3.1	Sample Preparation	14
3.1.1	Silver (Ag)	14
3.1.2	Magnesium Oxide (MgO)	15
3.1.3	Pentacenequinone	16
3.1.4	2-Hydrogen Phthalocyanine	17
4	Results	19
4.1	Pentacenequinone	19
4.2	2-Hydrogen Phthalocyanin on Ag(100)	20
4.3	Magnesium-Oxide (MgO)	22
4.4	2-Hydrogen Phthalocyanine on MgO	23
5	Discussion	27
5.1	2HPC/Ag(100)	27
5.2	2HPC/MgO(100)/Ag(100)	27
	Bibliography	29

Introduction

The study of molecular adsorption on solid surfaces is an important and influential field within surface science. This thesis is a comprehensive exploration of the adsorption behaviour of two organic molecules, Pentacenequinone (PQ) and 2 Hydrogen Phtalocyanine (2Hpc), on Ag(100) and MgO(100)/Ag(100). The present study delves into the phenomenon of Fractional and Integer Charge Transfer (FCT and ICT) and the formation of ordered structures. Organic molecules with semi-conductive properties such as 2Hpc, exhibit significant potential in opto-electronic technologies. The enhancement of device efficacy and functionality is reliant on their surface interactions. Furthermore Phthalocyanines are used as enzyme-like catalysts , liquid crystals, in photovoltaic cells or as photodynamic reagents for cancer therapy. [21] The versatility of these molecules arises from their ability to form coordination complexes with metals, giving them the name Metal-Phthalocyanines (MPc).[21] This process can change their optical or electronic properties, while leaving the inherent geometric structure unchanged [21]. Hence, it is important to understand the intricacies of their adsorption behavior, charge transfer mechanisms, and structural order formation to achieve technological progress.

For 2H-tetraphenylporphyrin (2H-TPP), a molecule similar to 2Hpc, self metallation has been observed on MgO(100) thin films. [6] Interestingly, in this case charge transfer seems to play a crucial role in this process. In 2H-TPP the 4 peripheral phenyl rings are tilted relative to the plane of the molecular macrocycle, leading to a relativly high adsorption height of the macrocycle . Charge transfer transfer reduces this adsorption height, enabling self metallation (see Fig. 1.1).

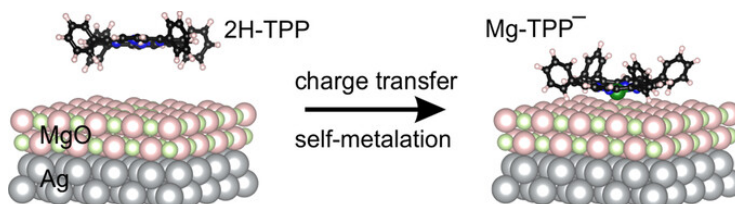


Fig. 1.1: Selfmetallation precess of 2H-TPP on MgO(100)/Ag(100) [6]

Naturally, this leads to the question whether those two processes, self-metallation and charge transfer, are also connected in such a way for completely flat molecules, such as 2Hpc. The aim of this thesis is to understand and categorize the adsorption behavior of both adsorbates on an Ag(100) single crystal and on a MgO(100) thin

film grown on Ag(100), with the main focus on 2-Hydrogen-Phthalocyanine (2HPc). PQ is exclusively imaged on Ag(100), where the focus is to observe bigger structures without imaging individual molecules.

Fundamentals

2.1 Scanning Tunneling Microscopy (STM)

The Scanning Tunneling Microscope was introduced in 1981 by Gerd Binning and Heinrich Rohrer. With this measuring technique it is possible to resolve a conductive surface with a precision far beyond that of conventional light based Microscopes. In contrast to other electron based microscopy like Scanning Electron Microscopes (SEM), it uses the quantum mechanical phenomenon of tunneling. In classical mechanics, objects cannot overcome a potential barrier if their energy E is smaller than the barrier $E < V_0$, as observed in gravitational interactions. This phenomenon observed for quantum mechanical particles like electrons, which can surpass a potential barrier despite the initial expectation for classical mechanics that they should not be able to. The STM uses this effect by precisely positioning a sharp conductive tip close to the surface and applying a bias voltage. The distance between the tip and the sample then represents the tunneling barrier. By varying the bias voltage, the tunneling probability can be changed, thereby affecting the tunneling current. If the bias voltage, also referred to as the potential difference, is kept constant, the tunneling current is primarily dependent on the distance between tip and surface. Thus the tip-sample distance can be accurately measured in the sub Ångström range by measuring the tunneling current. The tip is moved in the x-y-plane, where a grid is established, measuring the tip-sample distance for each grid point, a topographic image of the sample surface can be created. There are two modes of operation, the constant-height mode, where the tip is held at a constant height above the sample while scanning and the change in tunneling current is measured, and the constant-current mode, where the tip height is adjusted to keep the tunneling current constant during scanning.

The tunneling current is not only influenced by the sample geometry/topography, but also by the electronic structure of tip and sample. If the tip is in the vicinity of the metallic substrate the fermi energies align, resulting in an equal probability of electrons tunneling from the tip to the sample and vice versa. This consequently results in a zero net current. Through the introduction of a bias voltage U_{bias} the fermi energies of tip and sample can be shifted relative to each other (Figure 2.1). If the bias voltage is positive, the fermi energy of the sample is pushed down and electrons from occupied states in the tip can tunnel into the empty states of the sample. Consequently if the bias voltage is negative, electrons from the filled states of the sample tunnel into the tip. The tunneling current is influenced by the distance d between orbitals of the tip and the sample, which makes it possible to gain information about the electronic structure of the sample. This is not really a representation of the real structure of the atoms or molecules, but the electronic Local Density of States (LDOS) of the sample's surface. Utilizing this in Scanning Tunneling Spectroscopy (STS) provides additional information beyond the sample's topography, such as the chemical composition, bonding, the energy gap and band-bending effects. [1]

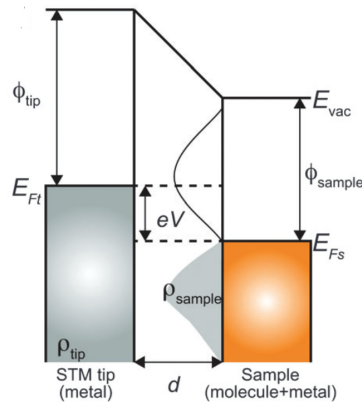


Fig. 2.1: Energy diagram of the tunneling junction with a positive bias voltage applied. Φ_{tip} & Φ_{sample} : work functions of tip and sample, E_{vac} : vacuum energy level, E_{ft} & E_{fs} : Fermi Energys of the tip and sample, ρ_{tip} & ρ_{sample} : density of states of tip and sample, eV : potential difference caused by applying a bias Voltage V (picture source: [9])

2.1.1 Theoretical Foundations of STM

A detailed description of the tip-sample interaction is provided by the model developed by Tersoff and Hamann. [19] Here, the tip is approximated as spherical potential well (Figure 2.2). R is in that case the radius of the tip located at position \vec{r}_0 with the distance d from the surface. First order perturbation theory then gives the following expression (Eq. 2.1) for the tunneling current of this system :

$$I = \frac{2\pi e}{\hbar} \sum_{\mu\nu} f(E_\mu)[1 - f(E_\nu + eV_{bias})] \cdot |M_{\mu\nu}|^2 \delta(E_\mu - E_\nu) \quad (2.1)$$

The fermi distribution $f(E) = (\exp((E-E_F)/k_bT)+1)^{-1}$ gives the occupation probability of a fermion (electrons) with the Energy E near the fermi level. In this case it is the occupation probability of the tip states (denoted by the subindex μ) and the occupation probability of the sample states (denoted by the subindex ν). The tunneling matrix $M_{\mu\nu}$ is related to the derivatives of the sample wave functions ψ_ν at the nucleus of the apex atom [4]. When STM Imaging is done at low temperatures and with small voltages, Equation 2.1 can be simplified to:

$$I = \frac{2\pi}{\hbar} e^2 V_{bias} \sum_{\mu\nu} |M_{\mu\nu}|^2 \delta(E_\nu - E_F) \delta(E_\mu - E_F) \quad (2.2)$$

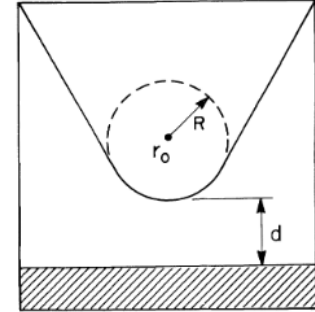


Fig. 2.2: Schematic depiction of the tip geometry [19]

With the tunneling matrix $M_{\mu\nu}$, which relates to the probability of an electron transitioning from state μ to state ν [4]. It is defined as the surface integral over the separation surface Σ , where $d\vec{S}$ is the surface element on Σ :

$$M_{\mu\nu} = \frac{\hbar^2}{2m} \int_{\Sigma} (\psi_\mu^* \vec{\nabla} \psi_\nu - \psi_\nu \vec{\nabla} \psi_\mu^*) d\vec{S} \quad (2.3)$$

To obtain a solution, the tip wave function can be explicitly chosen as an s-type orbital, which reduces complexity through the introduction of symmetry. This orbital has a spherical form [19]:

$$\psi_\mu = \Omega_t^{-1/2} * c_t k R e^{kR} (k|\vec{r} - \vec{r}_0|)^{-1} e^{-k|\vec{r} - \vec{r}_0|} \quad (2.4)$$

$\Omega_t^{-1/2}$ is the volume of the probe, $k = \hbar^{-1} \sqrt{2m\phi}$ is the inverse decay length for the wave functions in vacuum, c_t is a geometry specific constant on the order of 1 and R is the radius of curvature. The surface wavefunctions can be approximated as

blochwaves, which are plane waves modulated by a periodic function. In the region of negligible Potential the surface wavefunction can be written as:

$$\psi_\nu = \Omega_s^{-1/2} \sum_G a_G \exp(-(k^2 + |\vec{k}_{||} + \vec{G}|^2)^{1/2} z) \cdot \exp(i(\vec{k}_{||} + \vec{G}) \cdot \vec{x}) \quad (2.5)$$

Here $\Omega_s^{-1/2}$ is the sample volume, k the previously mentioned inverse decay length, $\vec{k}_{||}$ is the surface bloch wave vector and \vec{G} represents the reciprocal surface vector. Substituting into 2.2 gives the result:

$$I = 32\pi^3 e^2 V_{bias} \phi^2 D_t(E_F) R^2 k^{-4} e^{2kR} \cdot \sum_\nu |\psi_\nu(\vec{r}_0)|^2 \delta(E_\nu - E_F) \quad (2.6)$$

Where $D_t(E_F)$ is the Density of States of the Tip at the Fermi Level. The sum over the local states of the surface ψ_ν at the Fermi Level ($\delta(E_\nu - E_F)$) can be interpreted as the Local Density of States (LDOS). Using the surface wavefunction one can see that the tunneling current decreases exponentially with increasing tip sample distance d . Because of this exponential dependence, the tip height can be measured with such high precision. :

$$I \propto e^{-2 \cdot d \sqrt{\frac{2m\phi}{\hbar^2}}} \quad (2.7)$$

2.2 Low Energy Electrons Diffraction (LEED)

LEED is a simple technique that can image periodic structures present at the sample surface. A collimated beam of electrons with the same wavelength is directed at a flat surface. In this case the wavelength of the incoming electrons is determined by the electric field U_a that accelerates them (see Eq. 2.8). To see diffraction the wavelength of the electrons must be in the range of the lattice constant. The kinetic energy of the electrons is up to $E_{kin} = eU_a = 200$ eV.

$$\lambda = \frac{h}{\sqrt{2m_e e U_a}} \quad (2.8)$$

If a periodic structure is present at the surface, a sharp pattern of spots can be observed, which corresponds to the k-space of this structure. The LEED setup consists of a filament which emits electrons by applying a current. These electrons are then accelerated and collimated in a drift tube which points at the sample. Due to interactions of the electrons with the crystal atoms some of them are not diffracted elastically. To ensure that only the elastically scattered electrons are shown on the fluorescent screen, a grid system is installed in front of the screen. The first grid and the sample are both grounded to ensure that the diffracted electrons propagate undisturbed through the space between the sample and the grid. A filter voltage is applied between the second and third grid that is just below the acceleration voltage. Electrons which are not elastically scattered are completely stopped, which makes it effectively a high pass filter. [10]

The collimated beam can be represented as a planar wave $e^{i\vec{k}_0 \cdot \vec{r}}$ outside the surface. The wavevector \vec{k}_0 points in the propagation direction and represents the spatial frequency of the wave. This vector can be modeled as:

$$|\vec{k}_0| = \frac{2\pi}{\lambda} = \frac{\sqrt{2m_e E}}{\hbar} \quad (2.9)$$

$$\vec{k}_0 = \begin{pmatrix} |k_0| \cos(\varphi) \sin(\vartheta) \\ |k_0| \sin(\vartheta) \sin(\vartheta) \\ |k_0| \cos(\vartheta) \end{pmatrix} \quad (2.10)$$

A 2D periodic surface structure with a reciprocal basis (b_1, b_2) causes the plane waves to diffract. The diffracted waves are described as $A_g e^{i\vec{k}_g \cdot \vec{r}}$ with wave vectors $|\vec{k}_g| = |\vec{k}_0|$. \vec{k}_g transforms according to $\vec{k}_g = \vec{k}_0 + \vec{g}$. The reciprocal lattice vector $\vec{g} = 2\pi(hb_1 + kb_2)$ represents the individual points where constructive interference is present. Usually the indices h and k are integers which characterize the beam, for example $(0,0)$ or $(1,1)$. It can be shown that the wave vector in vacuum outside the surface is [10]:

$$k_g = -\sqrt{\frac{2m_e E}{\hbar^2} - (k_{0x} + g_x)^2 - (k_{0y} + g_y)^2} \quad (2.11)$$

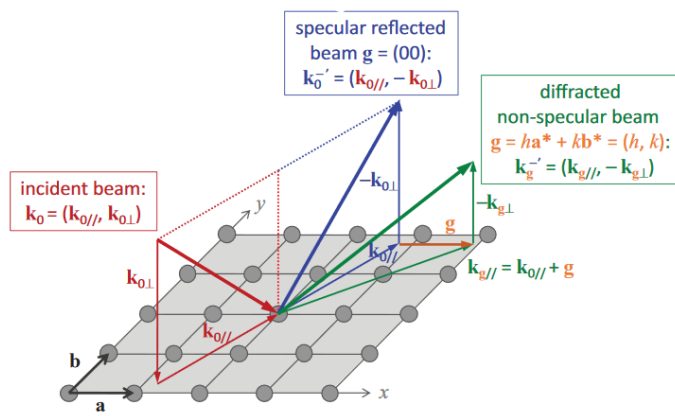


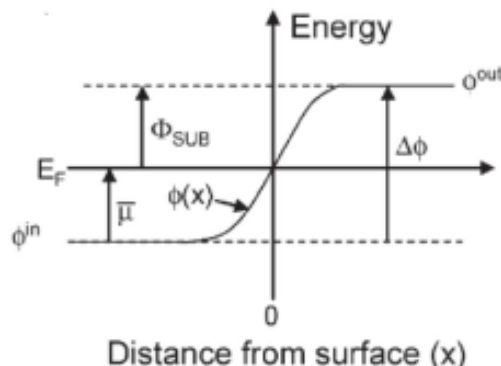
Fig. 2.4: 2D lattice with the reciprocal lattice vectors \vec{a} and \vec{b} . \vec{k}_0 (red): incident beam, \vec{k}_0' (blue): specular reflected beam, \vec{k}_g' (green): non-specular diffracted beam, \vec{g} (orange): 2-D reciprocal lattice vector $\langle hk \rangle$. [10]

2.3 Energy Alignment

This section was heavily influenced by and based on the research presented in the PhD thesis of Michael Hollerer, titled "Charge Transfer through thin Dielectric Films: Organic Molecules on MgO(001)/Ag(001)". [8] The concept of energy level alignment is crucial for the understanding of adsorption of organic molecules on inorganic substrates like Ag or MgO. It can result in altered properties of molecules and can influence their electronic structure. Therefore it is subject of ongoing research. [3] As it is important for the explanation of some observed effects in the obtained experimental data a brief summary is provided.

The energy needed for extraction of an electron from a solid to a point in the vacuum far from the surface is defined as the workfunction. It is defined as the sum of the bulk chemical potential μ and the electrostatic surface dipole $\Delta\phi$.

$$\Phi = -\mu + \Delta\phi \quad (2.12)$$



In metals the electrostatic potential arises from electron spill-out which creates a dipole at the surface. While the local workfunction can vary depending on the local structure, it is averaged at further distances which gives rise to the global workfunction. For single crystal metals this energy can vary depending on the crystal plane exposed to the vacuum, and is mostly influenced by how closely packed it is. Mathematically, it can be expressed as the difference between the vacuum energy level and the Fermi energy:

$$\phi = E_{Vac} - E_F \quad (2.13)$$

This even holds true for insulators like like MgO and other oxides with a large band gap. In metals the density of states is continuous around the fermi energy, which makes electronic states available for conduction. The occupation of states around E_F follows the Fermi-Dirac-Distribution and is influenced by the temperature. Organic Molecules on the other hand have discrete energy levels for orbitals, with the most important for adsorption being the Highest Occupied Molecular Orbital (HOMO) and the Lowest Unoccupied Molecular Orbital (LUMO). The energy gained by bringing

an electron from the vacuum energy level to the LUMO energy level is called the Electron Affinity (EA), while the energy needed to bring an electron from the HOMO to the vacuum level is called the Ionisation Energy (IE). When a molecule is adsorbed onto the surface the vacuum levels of the substrate and the molecule align. If the substrate has a high workfunction and the molecules Electron Affinity is smaller, the molecule will most likely adsorb in a neutral charge state. If on the other hand the molecules EA is high enough, or the substrate work function low enough, the LUMO is pushed under the Fermi-Energy Level, which means that charge transfer into the LUMO will occur. This is due to the fact that all states below E_F are occupied.

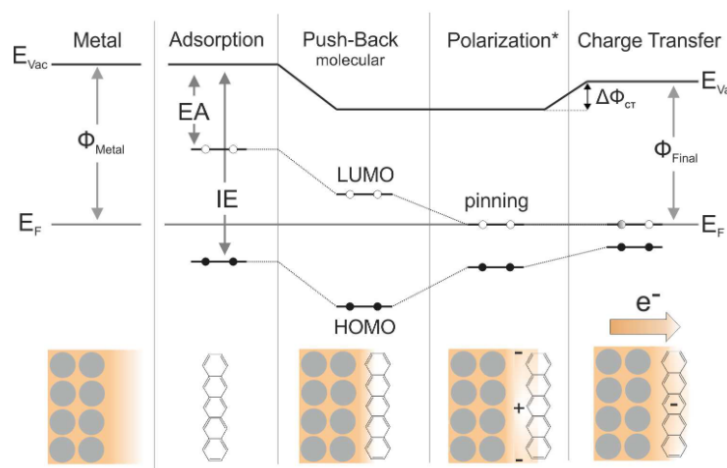


Fig. 2.6: Energy Level Alignment process of an organic molecule (Pentacene) adsorbed onto a metal substrate. [8]

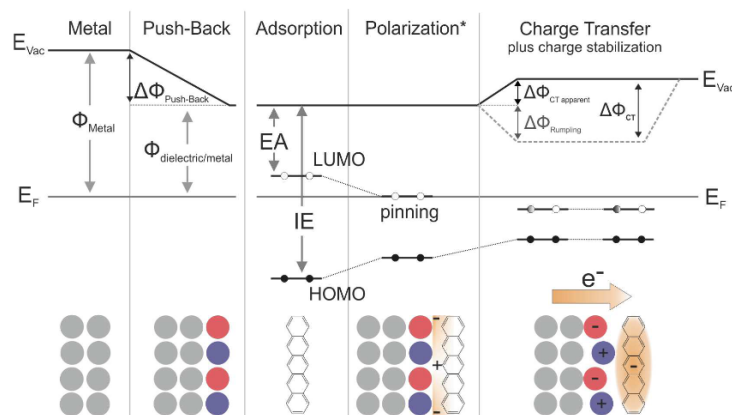


Fig. 2.7: Energy Level Alignment process of an organic molecule (Pentacene) adsorbed onto a dielectric/metal substrate. Note that the push-back effect arises from the dielectric/metal interaction.[8]

2.3.1 Push-Back

As discussed earlier, a non-zero negative charge is observed outside the surface. This is commonly known as the electron spill-out and results in an electric dipole, which in turn contributes to the work function of the substrate. Upon adsorption of the molecule, the electronic states interact, leading to Pauli Repulsion. This, in turn, pushes the charge back into the surface and reduces the electric dipole, consequently reducing the work function in respect to the Fermi Energy.

2.3.2 Polarization

The surface charges rearrange upon adsorption of a polarizable molecule, which intern manifests in an attractive interaction with unoccupied states and an repulsive interaction with occupied states. This results in a decrease of the LUMO-HOMO gap in respect to the gas-phase LUMO-HOMO gap of the adsorbates. In this process the workfunction of the substrate does not change, because no overall dipole perpendicular to the surface is introduced.

2.3.3 Charge-Transfer (CT)

If the LUMO is shifted below the Fermi Energy (E_F) of the metal substrate, it becomes (partially) occupied. This is due to the fact that metals have a continuous density of states at E_F with no bandgap. The molecules frontier orbitals therefore hybridize with the metal states resulting in an overlap of the molecular wavefunctions with a corresponding substrate state. This results in partial occupation of the LUMO, which is referred to as Fractional Charge Transfer (FCT) [17]. If looking at thin dielectric films on metal substrates like MgO on Ag, no FCT is observed. In contrast to metals, dielectric materials do not have continuous DoS at the Fermi Level and therefore no states available for hybridization. For a low initial workfunction and a high EA like depicted in Fig 2.7 the LUMO is pushed below E_F . As a consequence of this, electrons will tunnel through the dielectric layer to occupy it. Electrons can only tunnel as a whole, and therefore it is referred to as "Integer Charge Transfer (ICT)". This leads to the formation of a surface dipole, which in turn increases the workfunction. It should be noted that the charge transfer from the molecule to the substrate is also possible if the IE is low and the initial workfunction is high. This workfunction increase then raises the LUMO energy, CT continues either until all available LUMOs are occupied, or the LUMO has been raised in energy up to E_F , at which point CT stops. This process is called Fermi-level pinning and will play a significant role in the explanation of observed phenomena in this thesis.

Experimental Setup

The experimental work done in this thesis primarily utilized a Low-Temperature Scanning Tunneling Microscope setup (LT-STM). This STM is composed of two distinct compartments, the preparation chamber (PC) and the measurement chamber (MC). The sample is inserted through an airlock into the preparation chamber. In the whole system Ultra High Vacuum (UHV) at about $10^{-11} - 10^{-10}$ mbar is maintained, which is achieved by four individual pumps. The base Vacuum is achieved with the turbomolecular pump and the scroll pump through the airlock. Additionally, there is a titanium sublimation pump and an ion pump in the preparation chamber.

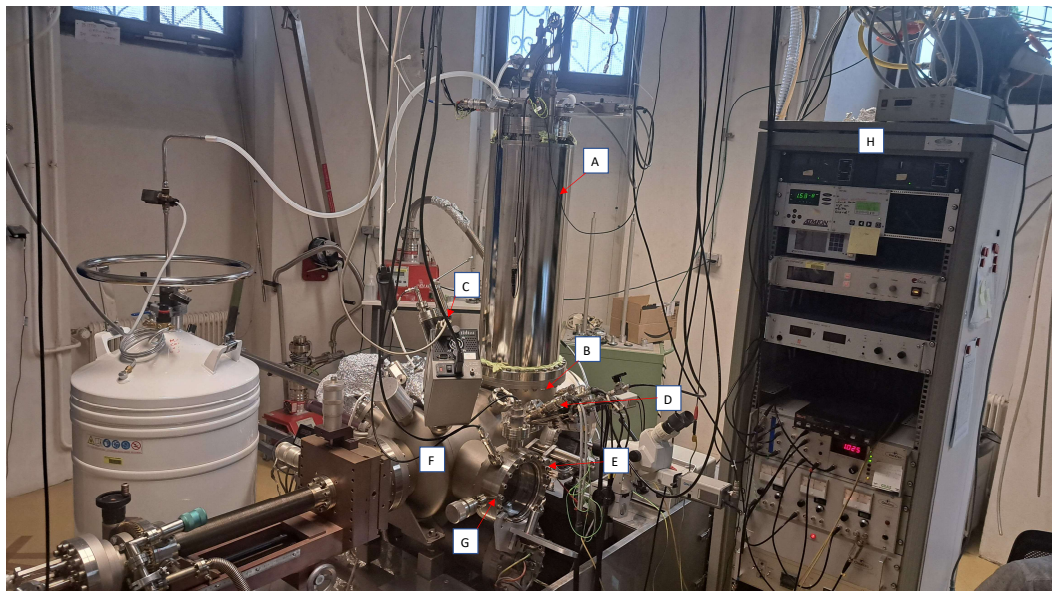


Fig. 3.1: The experimental setup used, A: cryostat filled with Liquid Nitrogen, B: measurement-chamber with spring suspended STM, C: sputter-gun, D: metal-evaporator, E: molecule-evaporator, F: preparation-chamber with sample manipulator, G: LEED system, H: Electronic used to monitor the function of the STM

The manipulator can be moved in each direction and rotated around its z-axis. It is also used to insert the Sample-holder into the STM. The PC contains a LEED

system, which fluorescent screen can be extended. Additionally the PC has a metal-evaporator (E-beam evaporator) and a organic-molecule evaporator (triple Knudsen cell) which are used for sample preparation. The sample is mounted onto the previously mentioned Sample-holder with a Heatwaves Labs Inc. button sample heater with a resistive heating range of 20 K - 900 K. The sample can also be cooled using LN₂ or LHe through a built-in pipe system in the manipulator arm. A Quartz-Crystal Microbalance (QCM) with sub Angström precision is used to monitor the deposition rate. To clean the sample, an Argon sputter gun is employed, which utilizes an electric field to ionize and accelerate argon gas. The MC consists of a LT-STM which is mounted to a two-shell cryostat, and surrounded by two radiation shields to achieve temperatures as low as 7 K, when cooled with Liquid Helium. In this thesis the cryostat chamber was filled with LN₂ which means it was operated at 75 K. The primary measuring unit (STM) is vibrationally damped using a coupled spring system.

3.1 Sample Preparation

3.1.1 Silver (Ag)

The Substrate used in this thesis is a Silver Ag(100) single crystal. Silver naturally crystallizes into a face centered cubic (fcc) structure with a lattice constant of $a = 4.079 \text{ \AA}$. [5] The single crystal is cut along the (100) plane giving it a square surface lattice along the [011] and [01\bar{1}] Direction, with a neares neighbor distance 2.884 Å. To ensure that the surface is clean, multiple cycles of Argon-Ion Sputtering with consequent annealing were performed. The first preparation was done with 3x Sputtering for 5 min each and annealing at 500 C° for 3-5 min. Later a longer sputtering time of 20 min proved more effective. Prior to the metal or organic adsorbtion the substate is cooled to room temperature.

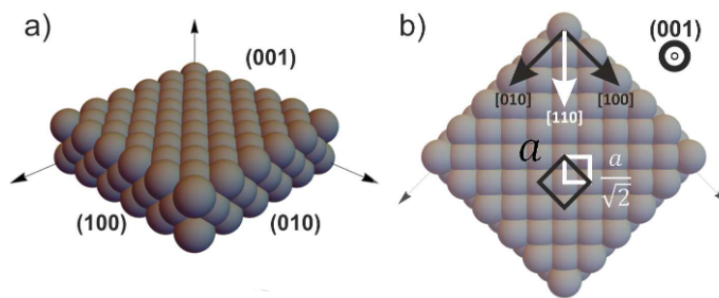


Fig. 3.2: (a) Crystal lattice structure of an fcc Ag single crystal sectioned along the (100) plane. (b) Top View with the depicted nearest neighbor distance of 2.884 Å[8]

3.1.2 Magnesium Oxide (MgO)

The crystal structure of MgO is fcc with a lattice constant of $a = 4.22 \text{ \AA}$ [7], which makes it only 3.4 % larger than Ag . This allows for the formation of ultrathin $\text{MgO}(100)$ films on $\text{Ag}(100)$, with relatively large, defect free terraces. The preparation on $\text{Ag}(100)$ is done using a E-beam evaporator, in which a filament is heated, causing it to emit electrons. These electrons are then accelerated using a high voltage (250-300V) onto the Magnesium crucible. The product of the emission current and acceleration voltage is the heating power. To ensure a monolayer the deposition rate is measured using a Quarz-Crystal Microbalance (QCM). A deposition rate of 0.5 $\text{\AA}/\text{min}$ is established. Magnesium is then deposited onto the $\text{Ag}(100)$ substrate, which is heated to 300 °C, while Oxygen O_2 is being fed into the Preparation Chamber (10^{-6} mbar). After the film is deposited, the sample is being slowly cooled at a cooling rate of 5 K/min to room temperature. This ensures larger terraces as MgO is known to break into small islands if cooled too fast. [15]

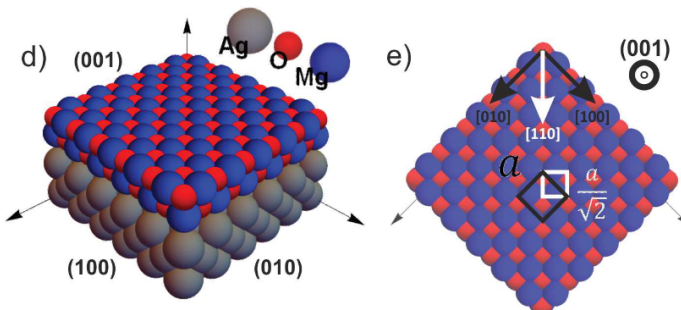


Fig. 3.3: (d) Crystal lattice structure of 2 ML $\text{MgO}(100)$ on $\text{Ag}(100)$ sectioned at the (100) plane, (e) Top View with the depicted nearest neighbor distance of $\frac{a}{\sqrt{2}}$ [8]

3.1.3 Pentacenequinone

Pentacenes are a organic molecule group with five linearly organised benzene rings, which share two neighboring carbon atoms. The carbon atoms are sp^2 hybridised, which gives it a hexagonal structure in which the single- and double-bond is alternating. The π orbitals extend out of the molecular plane. These overlapping π orbitals result in delocalized electrons, which makes it a conjugated π -bond system.

Quinone refers to the replacement of two hydrogen atoms with two oxygen atoms in a benzene ring. The two carbonyl groups ($C=O$) in this adsorbate are located on the central ring. Pentacene is an organic p-type semiconductor, which is used in the domain of organic electronics. It is remarkably stable and has a high charge mobility for an organic molecule of $2.2\text{ cm}^2\text{ V}^{-1}\text{ s}^{-1}$. [11] Pentacenequinone exhibits similar properties and is used as a precursor for the synthesis of pentacene.

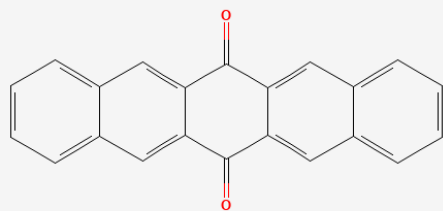


Fig. 3.4: The structure of Pentacenequinone [12]

3.1.4 2-Hydrogen Phthalocyanine

Phthalocyanines are a group of organic molecules that are structurally related to porphyrins and are mostly used as a blue pigment. [20] Other applications are nonlinear optical materials, enzyme-like catalysts, liquid crystals, sensitizers, photovoltaic cells or even as photodynamic reagents for cancer therapy. [21] They are characterized by a symmetric macrocyclic structure of four isoindole units $[(C_6H_4)C_2N]$, which consists of a pyrole unit fused with a benzene ring. The isoindole units are linked by four nitrogen atoms (aza-bridges) forming a conjugated ring. This allows delocalization of the π electrons across the macrocycle.

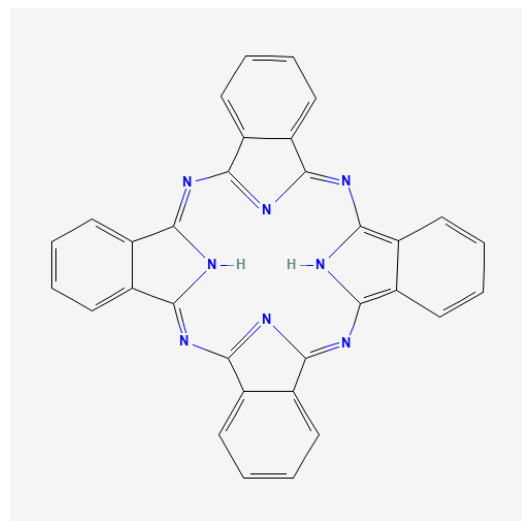


Fig. 3.5: The structure of 2-H Phthalocyanine [13]

There are more than 70 variations of phthalocyanines, with they key difference in the substitution of different elements or transition metals (e.g. Cu^{2+} and Ni^{2+}) in the middle of the molecule [20]. The physical properties can be altered by the choice of different metal ions, like the adsorption characteristics or the geometry of the molecule itself. In this thesis, 2-Hydrogen Phthalocyanine is studied, which harbors, two hydrogen Atoms in the middle of the Macrocycle attached to two opposing pyrole units. Generally Phthalocyanines are remarkably chemically and thermally stable [20]. This can be attributed to its

planar geometry and conjugated macrocycle. Phthalocyanines are used as dye for textiles and as inks because they strongly absorb light in the visible range especially in 620 - 750 nm regime, which makes them appear dark green-blue. They are also known for their optical, electronic and photo-electronic properties, all of which make them a promising chemiresistor sensor. Because of the semiconducting properties of phthalocyanines, their capability as a transistor, its use as liquid crystal display or its solar-cell applications are investigated.

Results

4.1 Pentacenequinone

In Figure 4.1 the STM Images of Pentacenequinone deposited on Ag(100) are shown. It appears that PQ forms irregular shaped islands. Also, the terasse edges appear rough compared to Ag(100) terasse edges, indicating the presence of a PQ layer. No smaller structures within the first layer or the island could be observed using STM, additionally LEED doesn't show any periodic structure. It therefore can be concluded that PQ doesn't form any periodic structure on Ag(100), consequently the focus of this thesis lies on the study of 2HPc.

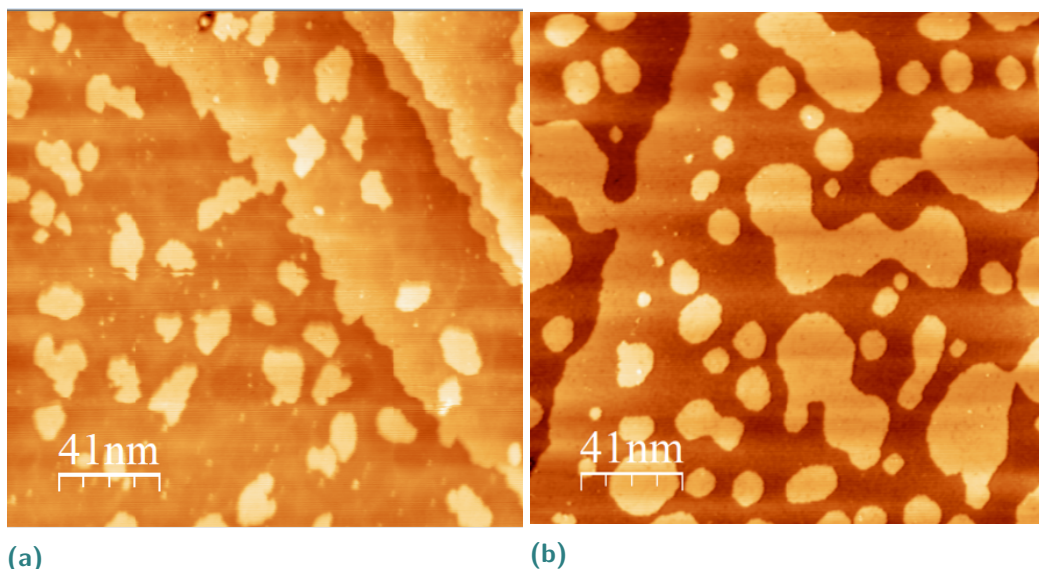


Fig. 4.1: 1 Monolayer + 2nd layer islands of pentacenequinone on Ag(100) $U_{bias} = 2 \text{ mV}$, $I = 8 \text{ nA}$

4.2 2-Hydrogen Phthalocyanin on Ag(100)

The STM and LEED Images of 2-Hydrogen Phthalocyanin (2HPc) on Ag(100) show the Formation of an ordered and almost defect-free structure. This indicates good mobility of the molecule during film growth. As seen in the Image 4.2 the 2HPc arranges in $\sqrt{3} \times \sqrt{3}$ R31 phase with an relative rotation of the molecular axis (MA) in respect to the [010] direction of $(11.6 \pm 1.2)^\circ$ (see figure 4.2).

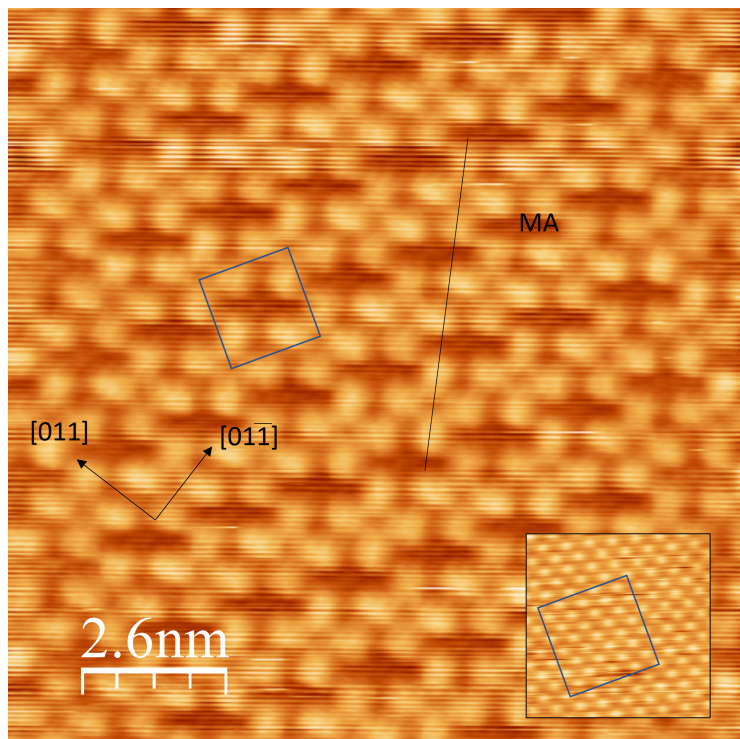


Fig. 4.2: STM image of 2HPc/Ag(100) taken in constant-current mode (monolayer regime). Image of Ag(100) at the same scale as reference . $U_{bias} = 480$ mV , $I = 0.05$ nA. MA: Molecular axis. blue square: unit cell of $\sqrt{3} \times \sqrt{3}$ R31 phase

At positive biasvoltages close to the fermi edge 2HPc appears as a cross with two opposing isoindole unit seemingly brighter than the other two. This is consistent with previous observation in literature for 2HPc on Ag(111), where the two bright isoindole units correspond to the two hydrogen atoms bound to the two pyrolic nitrogen atoms. [18] At negative biasvoltages close to the fermi edge the 2HPc Molecules appear as crosses with two fold symmetry, where two opposing isoindole units exhibit a different orbital structure than the other two. (see Figure 4.3a). This appearance is consistent with the 2HPc LUMO, calculated using DFT. [16] It is oriented in such a way that the benzene ring of one 2HPc molecule points towards the benzene ring of its nearest neighbor. As seen in Fig. 4.3a the LUMO can be observed near the Fermi Edge which suggests Fermi Level pinning.

This is most likely due to fractional charge transfer from the metal substrate , leading to an partially occupied LUMO and thus a charged molecule.

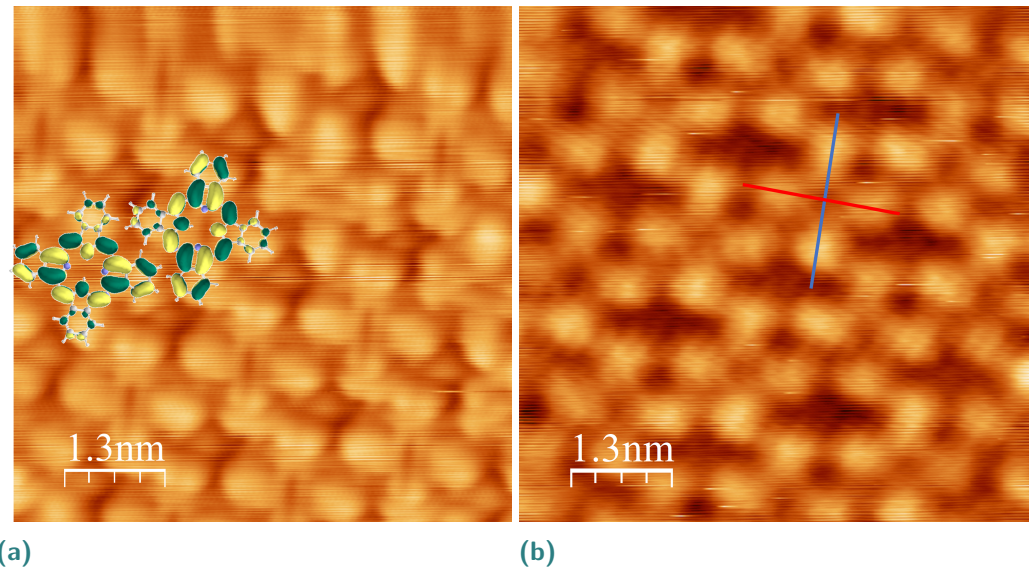


Fig. 4.3: (a) Constant-current image of 2Hpc/Ag(100). Two distinct LUMO orientations can be seen and their DFT-Simulation [16] counterparts. $U = -50.0$ mV , $I = 0.05$ nA. (b) Same spot imaged in constant-current mode at positive Bias-Voltages. $U_{bias} = 750$ mV , 0.02 nA.

In Figure 4.3b the same area as in Figure 4.3a is shown at large positive bias voltage, revealing unoccupied states in form of a two fold symmetric orbital.

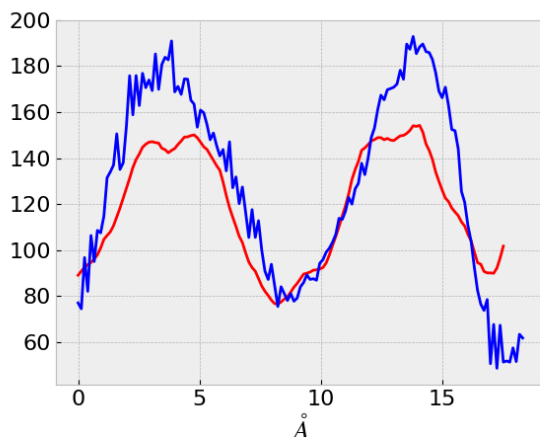


Fig. 4.4: Height profile plot, blue: vertical axis, red: horizontal axis

By looking at the pictures it is rather hard to see the brightness difference between the two pairs of isoindole units. In Fig 4.4 the intensity profile of the two perpendicular axis of the molecule shown in Fig 4.3b were investigated, which show significant brightness difference in the benzene ring locations. It is notable that the LUMOs axis is flipped 90° for some molecules when switching the polarity of the biasvoltage. There are two degenerated

LUMOs, with the electron density concentrated around two opposing isoindole units. This makes the Molecule reduce its symmetry from 4-fold to 2-fold. There is no

favored orientation seen in the STM images, which suggest that the occupation probability of the two LUMOs is the same.

4.3 Magnesium-Oxide (MgO)

Before depositing 2HPc (2H-phthalocyanine) on a MgO thin film, the quality of the surface was assessed using scanning tunneling microscopy (STM), followed by capturing a low-energy electron diffraction (LEED) image. The MgO forms sharp rectangular Islands with the edges along the [011] and [01 $\bar{1}$] directions as expected. In Figure 4.5 it can be seen that most of the islands are 15 - 20 nm wide. The Images show a MgO film consistent with literature.[22]

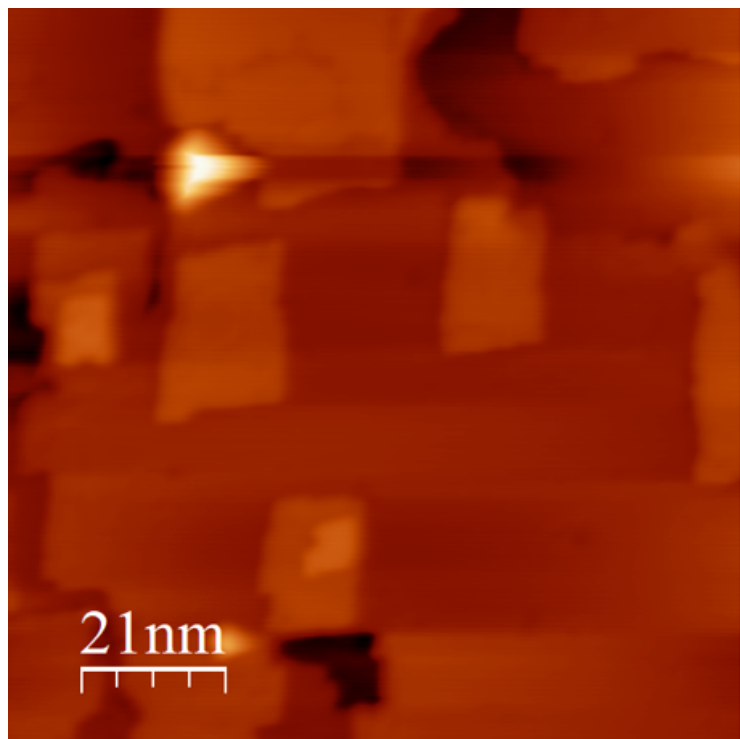


Fig. 4.5: Image taken at U_{bias} 3.5 V, most likely sub-monolayer to monolayer regime

4.4 2-Hydrogen Phthalocyanine on MgO

The STM images of 2HPc on MgO(100)/Ag(100) show again the formation of an ordered structure that persists across the the whole crystal lattice. Evident is the presence of linear defects, on which sites the 2HPc phase is shifted or even disconnected. This is most likely due to the fact that the underlying MgO long-range order is disturbed by the 3.2 % mismatch of the Ag an MgO lattice. Therefore resulting in incoherent sites, which give rise to intermediate phases with different orientation. In figure 4.6 the phase of the molecular adsorbate was determined. This was done using the Ag(100) lattice vectors, as they are almost identical to the MgO lattice. The superstructure of 2HPc on MgO(100)/Ag(100) was determined using a combination of STM and LEED measurements. The unit cell of 2HPc on MgO is rotated in direction of the [011] plane and is also larger than on Ag which can be attributed to the larger lattice constant. The phase was estimated to $\sqrt{40} \times \sqrt{40}R18.4$. In contrast to 2HPc on Ag(100) the molecule is mirrored in respect to the [001] plane with an molecular axis angle of $(1.9 \pm 1.4)^\circ$.

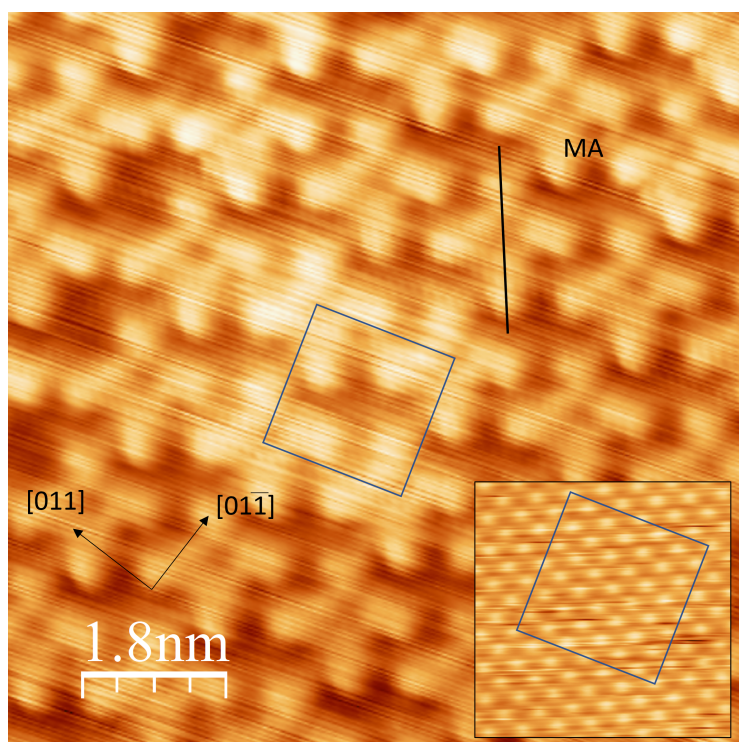


Fig. 4.6: STM image of 2HPc on MgO(100)/Ag(100) taken in constant-current mode (monolayer regime). Image of Ag(100) at the same scale as reference . U = 200 mV , I = 1 nA. MA: Molecular axis. blue square: unit cell of $\sqrt{40} \times \sqrt{40}R18.4$ phase

For further verification of the observed structure a LEED picture at 15 eV was taken after analysis with the STM. The LEED clearly supports the mainly observed phase,

but appeared diffuse which can come from additional phases or additional diffraction caused by the molecular structure. Additionally a 2D-FFT was performed on the STM image in figure 4.6 ,which aligns nicely with the observed LEED image.

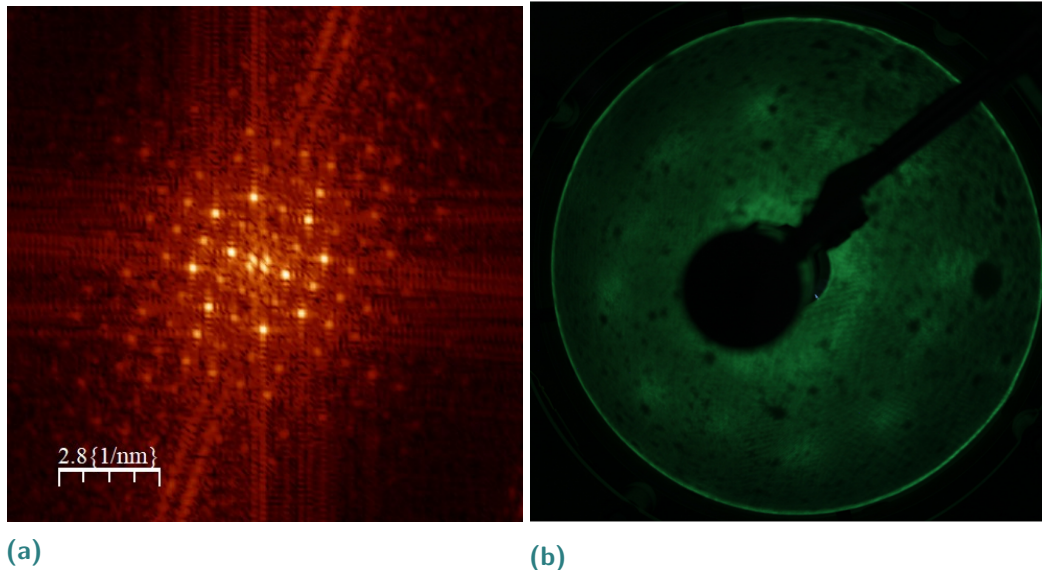


Fig. 4.7: (a) 2D-FFT of image in 4.6, (b) LEED picture taken at $E_{kin} = 15$ eV

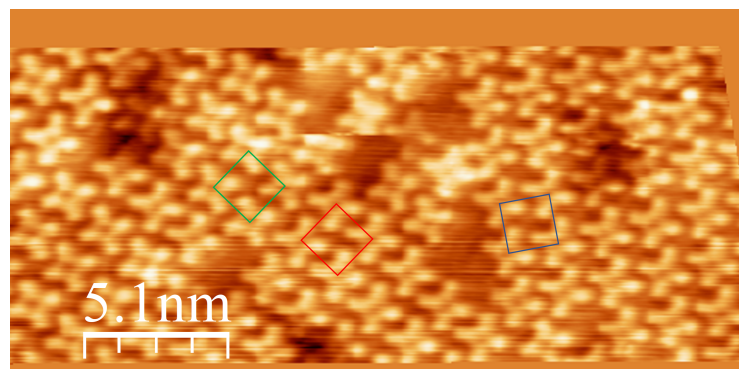


Fig. 4.8: Additional phases observed for 2HPc on $\text{MgO}(100)/\text{Ag}(100)$.

As seen in Fig. 4.8 there are three additional phases with two of them (red and green) aligned at the high symmetry direction [110], but different molecular orientation. The unit cells all have the same size.

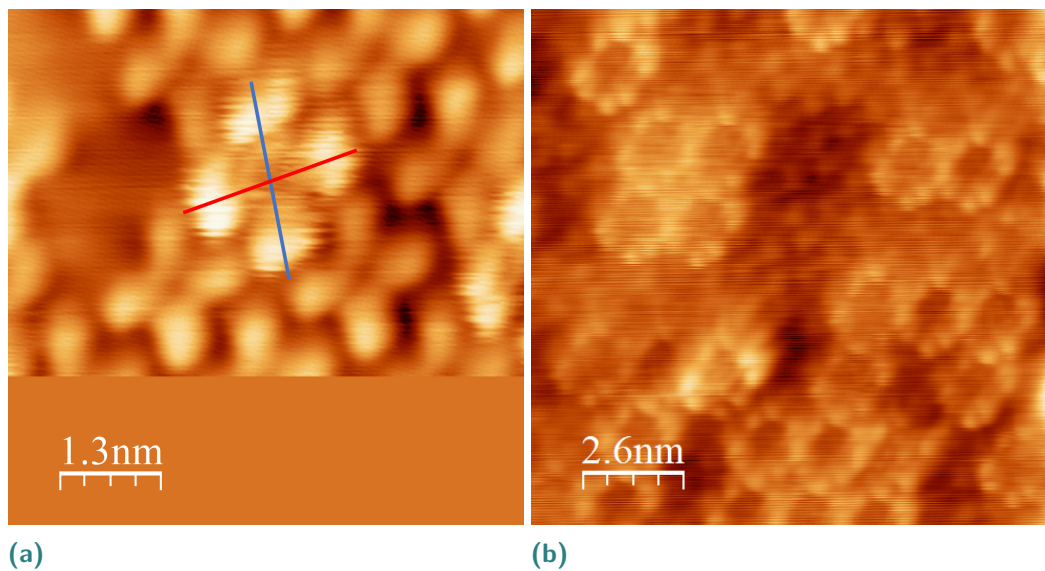


Fig. 4.9: (a) Image taken of a charged molecule at $U_{bias} = -250$ mV $I = 0.06$ nA ,
(b) charged molecule clusters at $U_{bias} = 700$ mV , $I = 0.07$ nA

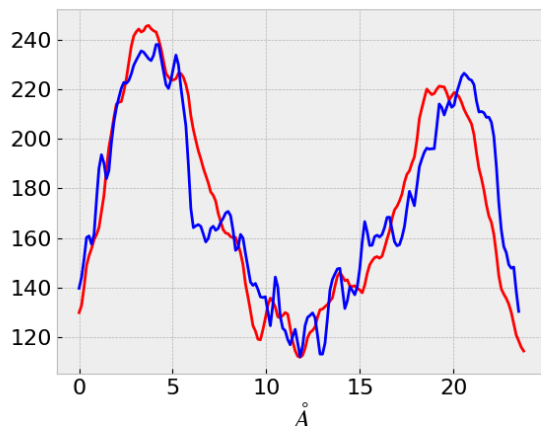


Fig. 4.10: Intensity profile plot, blue: vertical axis,
red: horizontal axis

The image depicted in Figure 4.9a was captured below the Fermi Energy level. It appears to feature a singly charged molecule, despite lacking the anticipated 2-fold symmetry observed in the calculated LUMO. This cannot be easily explained with the available data. These "rings" are also seen for distinct positive bias voltages, which indicates SOMO/SUMO splitting of the molecules LUMO. These two secluded states are seen for biasvoltages greater than 430

mV and less than -250 mV. Further investigation is needed to fully understand these complex electronic structures.

Discussion

5.1 2HPc/Ag(100)

Observation of one Phase:

The molecule is mainly observed in a $\sqrt{34} \times \sqrt{34}$ R31 phase with a molecular axis rotated $(11.6 \pm 1.2)^\circ$ relative to [010] (vertical direction). Interestingly the Molecular Axis doesn't line up with the [010] and [001] direction of the underlying silver lattice. This may indicate significant interactions between the nearest molecular neighbors.

Charge Transfer and Symmetry Reduction

The data indicates the shifting of the LUMO under the Fermi Level. This consequently leads to charge transfer that is observed as a partially occupied LUMO. The LUMO is seen well near the Fermi Energy, which indicates Fermi Level pinning. Furthermore the LUMO is also seen for positive bias which supports that it is partially occupied. The occurrence of partially charged molecules leads to symmetry reduction from C_4 (four-fold) to C_2 (two-fold). It is notable that for some molecules the direction of the prominent LUMO lobe is switched for positive biases and vice versa. This may come from the degeneracy of the LUMO which has two flipped Orbitals that have an angle of 90° in respect to each other. Therefore leading to a splitting of the degenerate energy levels and a more energetically favourable orbital to tunnel in to. Further investigation is needed to categorize this effect.

5.2 2HPc/MgO(100)/Ag(100)

The 2HPc/MgO/Ag system gives rise to surprising phenomena that deviates from the expected observation.

Observation of multiple Phases:

In contrast to 2HPc on Ag(100) there are at least three distinct phases, that are seen on the MgO film. The observation of multiple phases of 2HPc on MgO indicates a more complex adsorption behaviour on the dielectric film than on Ag(100). Additionally there are more defects present, which can be explained by the incoherent boundaries between Ag(100) and MgO(100).

ICT and SOMO/SUMO splitting:

Our results show that 2HPc exhibits a different electronic structure upon adsorption

on MgO(100) than on Ag(100). This can be explained by the commonly known Integer Charge Transfer through the thin dielectric layer. This results in an SOMO/SUMO splitting and could provide valuable insights in similar molecular systems.

Symmetry Change:

An unexpected observation was the deviation from the 2-fold symmetry expected for a charged molecule on MgO(100). As seen in Fig. 4.9 an unexpected four-fold symmetry is observed, which could be a hint for a metallation process occurring. This deviation could not be explained with the collected data and warrants further investigation.

Bibliography

- [1] Chunli Bai. *Scanning Tunneling Microscopy and Its Application*. Ed. by Springer. Shanghai Scientific and Technical Publishers, 1992 (cit. on p. 4).
- [2] Gerd Binnig, Heinrich Rohrer, Ch Gerber, and Edmund Weibel. „Surface studies by scanning tunneling microscopy“. In: *Physical review letters* 49.1 (1982), p. 57 (cit. on p. 3).
- [3] Slawomir Braun, William R Salaneck, and Mats Fahlman. „Energy-level alignment at organic/metal and organic/organic interfaces“. In: *Advanced materials* 21.14-15 (2009), pp. 1450–1472 (cit. on p. 9).
- [4] Julian Chen. „Tunneling matrix elements in three-dimensional space: The derivative rule and the sum rule“. In: *Physical review. B, Condensed matter* 42 (Dec. 1990), pp. 8841–8857. DOI: [10.1103/PhysRevB.42.8841](https://doi.org/10.1103/PhysRevB.42.8841) (cit. on p. 5).
- [5] Wheeler P. Davey. „Precision Measurements of the Lattice Constants of Twelve Common Metals“. In: *Phys. Rev.* 25 (6 June 1925), pp. 753–761. DOI: [10.1103/PhysRev.25.753](https://doi.org/10.1103/PhysRev.25.753) (cit. on p. 14).
- [6] Larissa Egger, Michael Hollerer, Christian S Kern, et al. „Charge-Promoted Self-Metalation of Porphyrins on an Oxide Surface“. In: *Angewandte Chemie International Edition* 60.10 (2021), pp. 5078–5082 (cit. on p. 1).
- [7] IF Guiliatt and NH Brett. „Lattice constant variations in finely divided magnesium oxide“. In: *Transactions of the Faraday Society* 65 (1969), pp. 3328–3333 (cit. on p. 15).
- [8] Michael Hollerer. „Charge transfer through thin dielectric films: organic molecules on MgO (001)/Ag (001)/submitted Dr. rer. nat. of Michael Hollerer“. In: (2019) (cit. on pp. 3, 9, 10, 14, 15).
- [9] Shinya Kano, Tsukasa Tada, and Yutaka Majima. „Nanoparticle characterization based on STM and STS“. In: *Chem. Soc. Rev.* 44 (Oct. 2014). DOI: [10.1039/C4CS00204K](https://doi.org/10.1039/C4CS00204K) (cit. on p. 4).
- [10] Wolfgang Moritz. *Surface Structure Determination by LEED and X-rays*. eng. Cambridge: Cambridge University Press, 2022 (cit. on pp. 7, 8).
- [11] María L. Mota, Bibiana Rodriguez, Amanda Carrillo, et al. „Fast and inexpensive synthesis of pentacene with high yield using 6,13-pentacenequinone as precursor“. In: *Journal of Molecular Structure* 1154 (2018), pp. 511–515. DOI: <https://doi.org/10.1016/j.molstruc.2017.10.070> (cit. on p. 16).

- [12] National Center for Biotechnology Information (2023). PubChem Compound Summary for CID 76415, 6,13-Pentacenequinone. URL: https://pubchem.ncbi.nlm.nih.gov/compound/6_13-Pentacenequinone (cit. on p. 16).
- [13] National Center for Biotechnology Information (2023). PubChem Compound Summary for CID 86280045, Phthalocyanine. URL: <https://pubchem.ncbi.nlm.nih.gov/compound/Phthalocyanine> (cit. on p. 17).
- [14] R. Otero, A.L. Vázquez de Parga, and J.M. Gallego. „Electronic, structural and chemical effects of charge-transfer at organic/inorganic interfaces“. In: *Surface Science Reports* 72.3 (2017), pp. 105–145. DOI: <https://doi.org/10.1016/j.surfrep.2017.03.001> (cit. on p. 3).
- [15] Jagriti Pal, Marco Smerieri, Edvige Celasco, et al. „Morphology of monolayer MgO films on Ag (100): switching from corrugated islands to extended flat terraces“. In: *Physical Review Letters* 112.12 (2014), p. 126102 (cit. on p. 15).
- [16] Peter Puschnig. *Organic Molecules Database*. Accessed: 2021-05-26 (cit. on pp. 20, 21).
- [17] Sabine-A Savu, Giulio Biddau, Lorenzo Pardini, et al. „Fingerprint of fractional charge transfer at the metal/organic interface“. In: *The Journal of Physical Chemistry C* 119.22 (2015), pp. 12538–12544 (cit. on p. 11).
- [18] Alexander Sperl, Jörg Kröger, and Richard Berndt. „Controlled metalation of a single adsorbed phthalocyanine“. In: *Angewandte Chemie International Edition* 23.50 (2011), pp. 5294–5297 (cit. on pp. 3, 20).
- [19] J. Tersoff and D. R. Hamann. „Theory and Application for the Scanning Tunneling Microscope“. In: *Phys. Rev. Lett.* 50 (25 June 1983), pp. 1998–2001. DOI: [10.1103/PhysRevLett.50.1998](https://doi.org/10.1103/PhysRevLett.50.1998) (cit. on p. 5).
- [20] Arthur L Thomas. *Phthalocyanine research and applications*. CRC Press, 1990 (cit. on pp. 3, 17).
- [21] Yongfeng Wang, Kai Wu, Jörg Kröger, and Richard Berndt. „Structures of phthalocyanine molecules on surfaces studied by STM“. In: *AIP Advances* 2.4 (2012) (cit. on pp. 3, 1, 17).
- [22] Chaoqiang Xu, Yande Que, Yuan Zhuang, et al. „Manipulating the Edge of a Two-Dimensional MgO Nanoisland“. In: *The Journal of Physical Chemistry C* 123 (July 2019). DOI: [10.1021/acs.jpcc.9b04906](https://doi.org/10.1021/acs.jpcc.9b04906) (cit. on p. 22).